JEE Journal of Ecological Engineering

Journal of Ecological Engineering, 2026, 27(6), 148–162
https://doi.org/10.12911/22998993/216358
ISSN 2299–8993, License CC-BY 4.0

Received: 2025.11.28
Accepted: 2026.04.16
Published: 2026.05.01

Facile synthesis of ZnO/JBW zeolite composite derived from feldspar for efficient photocatalytic degradation of Rhodamine B

Julista Alfa Kabalmay[1], Paulina Taba[1*], Muhammad Zakir[1], Syarifuddin Liong[1], Nur Umriani Permatasari[1], Syahruddin Kasim[1], Rahmaniah Zainuddin[2]

[1] Department of Chemistry, Faculty of Mathematics and Natural Sciences, Hasanuddin University, Makassar 90245, South Sulawesi, Indonesia
[2] Department of Chemistry, Faculty of Mathematics and Natural Sciences, Universitas Gadjah Mada, Sekip Utara, Yogyakarta 55281, Indonesia
* Corresponding author e-mail: paulinataba@unhas.ac.id

ABSTRACT

The integration of ZnO with zeolitic frameworks offers a promising approach to developing composite photocatalysts with improved efficiency for advanced oxidation processes. In this research, JBW zeolite was produced from natural feldspar via a hydrothermal method and utilized as a substrate for synthesizing a ZnO/JBW composite. Structural and morphological analyses conducted through XRD, FTIR, SEM–EDS, TGA/DSC, and BET confirmed the successful creation of a crystalline JBW framework and uniform dispersion of ZnO within the structure, leading to improved surface properties and increased porosity. Optical evaluations of ZnO and ZnO/JBW using UV–DRS indicated a red shift in the absorption edge and a decrease in band gap energy from 3.18 eV to 3.12 eV, thereby enhancing light-harvesting efficiency. The photocatalytic activity was assessed using Rhodamine B as a representative pollutant under UV light exposure. Under optimal settings of pH 8, 20 mg/L Rhodamine B (RhB), and 150 minutes of irradiation, the ZnO/JBW composite achieved a degradation rate of 98%, while pure ZnO only attained 65%. This improvement was attributed to the synergistic effect arising from JBW adsorption and ZnO photocatalytic oxidation, which promoted effective charge separation and increased photocatalytic performance. The results highlight that ZnO/JBW is an economical, eco-friendly photocatalyst with significant potential for use in wastewater treatment and the removal of dye pollutants.

Keywords: ZnO/JBW composite, JBW zeolite, feldspar, photocatalysis, Rhodamine B, wastewater treatment.

INTRODUCTION

Industrial effluents that contaminate water sources have been recognized as one of the most pressing global environmental issues. Among various pollutants, Rhodamine B (RhB) dyes have been classified as highly toxic due to their carcinogenic properties and strong resistance to natural biodegradation processes (Al-Buriahi et al., 2022; Wang et al., 2020). Substantial amounts of RhB have been discharged from industries such as textiles, printing, and paper manufacturing units, where conventional methods of treatment, such as coagulation, biodegradation, and adsorption, have often failed to achieve complete mineralization (Al-Tohamy et al., 2022). According to environmental standards defined by the European Water Framework Directive, RhB concentrations above 14 µg/L *annual average* and 140 µg/L *allowable* are considered potentially toxic to aquatic ecosystems (Skjolding et al., 2021). Accordingly, there is a strong need for affordable and environmentally responsible technologies to achieve efficient elimination of persistent organic contaminants.

Advanced oxidation processes (AOPs), especially those based on semiconductor photocatalysis, have been widely acknowledged as effective approaches for degrading organic pollutants in wastewater. Photocatalysts can degrade dye molecules into non-toxic final products such as CO_2 and H_2O when exposed to UV or solar light (Goodarzi et al., 2023). Among commonly used semiconductors, zinc oxide (ZnO) stands out for its low cost, high oxidation potential, non-toxicity, and relatively simple preparation routes (Aina et al., 2025). Despite these advantages, the practical application of ZnO is limited by several intrinsic drawbacks. Its wide band gap confines photoactivity to the UV region, while the rapid recombination of photogenerated electron–hole pairs significantly hinders photocatalytic efficiency. Continuous irradiation may also lead to particle aggregation and photocorrosion, further reducing performance (Singh et al., 2025). To mitigate these issues, a range of modification strategies has been explored, including hybridization with metals (Bilal et al., 2025; Packialakshmi et al., 2023), other semiconductor oxides (Wei et al., 2025), carbon-based materials (Bekele et al., 2025; Rajendran et al., 2025), and various porous supports (Shamsaei et al., 2022; Soliman et al., 2022). Among these supports, zeolitic materials have gained particular attention. Their high surface areas, ion-exchange properties, and well-defined microporous channels promote uniform ZnO dispersion and improve pollutant adsorption. In addition, the rigid zeolitic framework can stabilize ZnO particles, thereby reducing aggregation and photocorrosion during photocatalytic operation. Overall, coupling ZnO with zeolitic materials offers an efficient strategy to mitigate the intrinsic drawbacks of pure ZnO and significantly improve its photocatalytic performance.

Zeolites are crystalline aluminosilicates with ordered microporous frameworks, and are widely regarded as excellent adsorbents, ion exchangers, and solid catalysts (Hübner et al., 2024). Their high surface area, adjustable pore morphology and size, and thermal and chemical stability create highly favorable conditions for immobilizing semiconductor particles. The fusion of ZnO semiconductor particles with zeolites has been shown to improve photocatalytic activity through synergistic adsorption (zeolites) and photocatalytic oxidation (ZnO) (Bilal et al., 2025; Packialakshmi et al., 2023). While many zeolites with framework types such as sodalite (SOD), cancrinite (CAN), or mordenite (MOR) have been investigated and analyzed for many of their applications, studies on JBW zeolites are untried for semiconductor-zeolites hybrids. The JBW zeolite derives its name from the Linde type J framework and the initials of Barrer and White, who originally identified it as a nepheline hydrate (Asselman et al., 2022). It is a metastable zeolite form mostly isolated under mild hydrothermal synthesis and features lath-like morphology and pseudo-hexagonal cross-sections. The moderate Si/Al ratio and the open-framework structure of JBW highlight its promise as a support material (Yan et al., 2024).

The synthesis of JBW zeolite from natural minerals such as feldspar offers a sustainable and cost-effective approach to zeolite production. Feldspar, a common aluminosilicate mineral, provides significant amounts of silicon and aluminum, which can be liberated by acid treatment and subsequently converted into zeolitic phases via hydrothermal synthesis (Khaleque et al., 2020). Although JBW has been successfully generated from kaolinite, earlier research has primarily focused on phase formation and ion-exchange capabilities. For instance, Lin et al. (2004) successfully obtained zeolites with JBW, CAN, Li-ABW, and SOD phases from meta-kaolinite, and Hegazy et al. (2012) produced phase-pure JBW and assessed its heavy-metal adsorption properties. However, these studies did not consider feldspar as a precursor, nor did they examine JBW for photocatalytic uses. Therefore, a notable research gap remains regarding the synthesis of feldspar-derived JBW, its potential as a ZnO support, and the performance of ZnO–JBW composites in degrading Rhodamine B.

In this context, incorporating ZnO into JBW zeolite prepared from feldspar can offer several noteworthy advantages. Owing to its interconnected, porous, and crystalline framework, JBW can disperse ZnO particles more evenly across its surface, thereby increasing the number of exposed active sites and minimising photocorrosion during irradiation. Another benefit arises from the complementary roles of the two components: while the zeolite framework can concentrate RhB molecules through adsorption, ZnO subsequently drives their oxidative degradation under UV light, resulting in a faster overall reaction. The use of feldspar as the starting material also provides a practical and environmentally considerate route for producing ZnO/zeolite composites. Findings from recent studies further show that ZnO–zeolite materials generally outperform either unmodified ZnO or pure zeolite in photocatalytic degradation tests (Bekele et al., 2025; Bilal et al., 2025).

Based on these considerations, this study focuses on the synthesis of feldspar-derived zeolite materials from Gowa Regency, Indonesia, and their application as supports for zinc oxide–based photocatalysts. The work is designed to investigate how the integration of ZnO with JBW zeolite and the operational conditions influence the structural–textural properties and photocatalytic behavior of the resulting composites in dye degradation systems.

MATERIALS AND METHODS

Materials

Natural feldspar was collected from Timbuseng, Pattalasang District, Gowa Regency, South Sulawesi, Indonesia. Zinc oxide (ZnO, CAS No. 1314-13-2, EMSURE® grade, ≥ 99.0% purity, Merck), Rhodamine B (RhB, $C_{28}H_{31}ClN_2O_3$, CAS No. 81-88-9, ≥ 95%, Sigma-Aldrich), sodium hydroxide (NaOH, CAS No. 1310-73-2, EMSURE® grade, ≥ 98%, Merck), ethanol (C_2H_5OH, CAS No. 64-17-5, EMSURE® grade, ≥ 96%, Merck), and hydrochloric acid (HCl, CAS No. 7647-01-0, EMSURE® grade, ≥ 37%, Merck). Deionized water was used throughout the experiments

Preparation of Feldspar

The feldspar raw material was crushed and sieved using a 200-mesh screen, 50 g of the sample was reacted with 100 mL of 1 M HCl under continuous stirring for 1 h. Afterward, the sample was washed with distilled water until it reached a neutral pH of 7 and subsequently oven-dried at 105 °C for a duration of 5 h.

Synthesis of JBW zeolite from feldspar

The zeolite was synthesized through the hydrothermal method by dissolving 1.025 g of NaOH in 18 g of deionized water. Subsequently, 0.7495 g of feldspar raw material was introduced into the mixture. The mixture was then placed within an autoclave, securely sealed, and subjected to heating at 170 °C for a duration of 72 h. The solid product obtained from the synthesis process was subsequently separated via vacuum filtration using filter paper until the filtrate attained a neutral pH (pH 7). The final product was then dried at 105 °C for a period of 12 h.

Synthesis of ZnO/JBW composite

The ZnO/JBW was obtained using a modified solid-state method, as reported by (Fatimah et al., 2025) and (Imessaoudene et al., 2024). Initially, 1 g of ZnO powder and 2.5 g of JBW were mixed with 4 mL of 96% ethanol and manually ground using an agate mortar. A volume of 21 mL of 96% ethanol was incorporated into the system, followed by 5 h of continuous agitation and 30 min of ultrasonic treatment to achieve a well-dispersed suspension. The obtained slurry was oven-dried at 105 °C for 5 h and then calcined at 400 °C for 2 h to produce the final ZnO/JBW composite.

Photocatalytic activity evaluation

The photocatalytic activity of JBW, ZnO, and ZnO/JBW was evaluated through the photodegradation of Rhodamine B (RhB) using a 500 W mercury lamp (λ = 365 nm). The pH optimization was carried out using RhB solution at a fixed concentration of 25 mg/L within the pH range of 4–9, while concentration experiments were performed at the optimum pH with variations of 10–35 mg/L; both sets of experiments were irradiated for 60 min. The time-dependent experiments was conducted at the optimum pH and concentration conditions with irradiation durations ranging from 30 to 180 minutes, and 4 mL aliquots were collected at 30-minute intervals. Before light irradiation, the suspensions used in the pH, concentration, and time-dependent experiments were stirred in the dark at 350 rpm for 30 min to achieve adsorption–desorption equilibrium of RhB on the catalyst. All collected samples were centrifuged at 3500 rpm for 10 minutes, and the aliquots were analyzed using a UV–Vis spectrophotometer at 555 nm. Equation 1 was used to determine the degradation efficiency:

$$\%D = \frac{C_o - C_e}{C_o} \times 100\% \tag{1}$$

where: C_o is the initial concentration and C_e is the final concentration of the dye. All photocatalytic experiments were performed in triplicate.

Characterization

Different analytical approaches were used to determine the physicochemical properties of the samples. Elemental composition was assessed by X-ray fluorescence analysis (Shimadzu EDX-/800). The crystallographic structure was determined by XRD (Shimadzu XRD-7000) with Cu Kα radiation (λ = 1.5405 Å) over a scanning range of 10–70° (2θ). Fourier-transform infrared spectroscopy (Shimadzu IR Prestige-21). Thermogravimetric and differential scanning calorimetry (PerkinElmer STA 8000). The Optical band gaps were measured using UV-DRS (Thermo Scientific Evolution 220). Morphology and elemental mapping were examined by SEM-EDS (Hitachi SU3500). N_2 adsorption–desorption (SAA Micro 200) with the BET and BJH methods.

RESULTS AND DISCUSSION

X-ray diffraction analysis

The diffraction patterns obtained from the untreated and acid-modified feldspar are presented in Figure 1. The XRD pattern of the raw feldspar in Figure 1a exhibited dominant reflections at 2θ = 19.9°, 23.6°, 27.3°, and 30.8°, corresponding to the (200), (130), (201), and (221) planes of feldspar (PDF 96-900-2566), along with quartz at 26.6° (101) and weak goethite peaks around 35°–37°. After activation with 1 M HCl Figure 1b the diffraction pattern remained dominated by feldspar with characteristic reflections between 20° and 31°, confirming that the aluminosilicate framework was preserved. The quartz peak intensity decreased, while the weak goethite reflections became less distinct, indicating partial dissolution of silica and removal of Fe-containing impurities. These results demonstrate that acid activation effectively purified the feldspar without altering its crystalline structure, producing a cleaner aluminosilicate precursor suitable for zeolite synthesis.

The XRD patterns of JBW, ZnO, and the ZnO/JBW composite are shown in Figure 2. The diffractogram was dominated by characteristic reflections of JBW zeolite, with major peaks at 2θ = 15.96°, 23.40°, 26.13°, and 30.16°, which correspond to the (200), (220), (310), and (321) diffraction planes (JCPDS 96-901-4434). These sharp and well-defined peaks confirm the successful formation of the JBW framework. The JBW phase is generally stable under low alkaline conditions, where Si and Al dissolution occur slowly, thereby favoring early-stage JBW nucleation before it transforms into other frameworks. Consistent with previous studies, low-alkalinity conditions were observed to promote the early crystallization of JBW prior to its transformation into more stable phase (Lin et al., 2004; Vogrin et al., 2023). The diffraction pattern of ZnO exhibited intense reflections at 2θ = 31.72°, 34.37°, 36.18°, 47.46°, 56.54°, 62,78°, 66.31° and 68.02°, which are assigned to the (100), (002), (101), (102), (110), (103), (200), and (112) lattice planes of the hexagonal wurtzite structure (JCPDS 96-230-0113).

The ZnO/JBW composite shows a diffraction pattern indicating an overlap of both phases. The ZnO reflections at 2θ = 31.72°, 34.37°, and 36.18°, with crystallographic planes (100), (002), and (101), are still clearly visible but show slight broadening due to interaction with the JBW matrix.The characteristic JBW reflections at 2θ = 23.40° and 26.13° corresponding to the planes (220) and (310), were still detectable, indicating that the JBW framework was preserved after ZnO incorporation. Variations in the intensities of the ZnO (100) and (101) planes, along with a decrease in the JBW (321) peaks, suggest interfacial interactions between ZnO and the aluminosilicate framework. Such intercations, likely involving Zn-O-Si/Al bonding at the interface, are expected to enhance both the thermal stability and photocatalytic properties of the composite (Khaleque et al., 2020; Shamsaei et al., 2022).

Composition and morphology

The chemical composition of the natural and acid-activated feldspar was examined through X-ray fluorescence (XRF) analysis, the results of which are presented in Table 1. The major oxides identified were Al_2O_3 and SiO_2, indicating that the feldspar mainly consists of aluminosilicate minerals. After activation with 1 M HCl, the concentrations of Al_2O_3 and SiO_2 slightly increased, whereas Fe_2O_3 and CaO decreased, suggesting the removal of Fe- and Ca-containing impurities during acid treatment. The XRD results corroborate these observations, demonstrating that feldspar persisted as the major phase after activation, accompanied by a reduction in the diffraction peaks of quartz and goethite. The reduction of Fe and Ca oxides detected by XRF supports the diminished impurity peaks observed in the XRD pattern.

The morphology and composition of the synthesized material were revealed by SEM-EDS, as presented in Figure 3. In the SEM images, Figure 3a shows elongated prismatic (lath-like) crystals with a characteristic pseudo-hexagonal cross-section typical of JBW zeolite. These crystals appear randomly distributed and exhibit micron-scale dimensions, consistent with previous reports (Asselman et al., 2022; de Dios et al., 2023; Hübner et

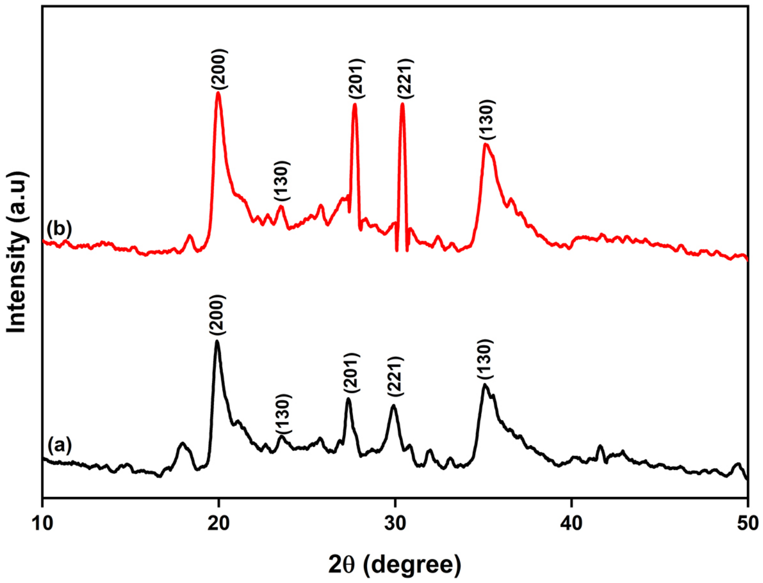

Figure 1. XRD patterns for (a) raw feldspar, and (b) the acid-activated feldspar

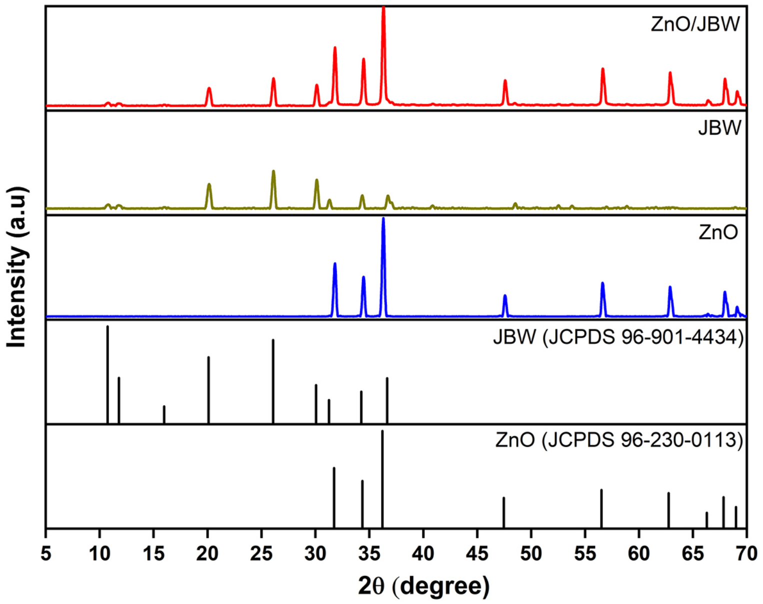

Figure 2. XRD patterns for ZnO, JBW, and the ZnO/JBW composite

al., 2024; Wei et al., 2025). The pseudo-hexagonal cross-section refers to crystal terminations resembling a hexagon, albeit not perfectly symmetrical, which is a common feature of JBW zeolite formed through hydrothermal synthesis. This morphology indicates a directional crystal growth aligned with the JBW framework topology. To further support morphological identification, EDS analysis (Figure 3b) was performed on the observed JBW crystals. The EDS spectrum confirmed the main elemental composition of Al (14.05%), Si (16.4%), Na (14.35%), and O (55.2%). The nearly balanced Al/Si ratio, along with the presence of Na as a charge-compensating cation, is consistent with the aluminosilicate framework of JBW zeolite. After composite with ZnO, the JBW morphology was still clearly identifiable. At the same time, ZnO particles were detected to be dispersed across the crystal surface (Figure 3c). This distribution was interpreted as an indication of strong interfacial interaction between ZnO and the JBW framework, which prevented particle agglomeration. The EDS spectrum (Figure 3d) confirmed the presence of Al (10.22%), Si (11.76%), Na (13.42%), O (46,85%), and Zn (15.88%), verifying the successful incorporation of ZnO into the

Table 1. Chemical composition of raw and acid-activated feldspar determined by XRF

Metal Oxide wt (%)	Raw feldspar	Acid-activated feldspar
$Al_{2O}3$	47.6	49.2
SiO_2	41.3	43.7
Fe_2O_3	4.1	3.5
CaO	3.9	0.6
K_2O	1.3	1.4
SO_3	0.4	-
MnO	0.1	-
PbO	0.01	-

JBW matrix. The detection of Zn suggested that JBW acted as both a structural support and a dispersing medium for ZnO.

Fourier transform infrared spectroscopy

The FTIR spectra of JBW zeolite, ZnO, and the ZnO/JBW composite are shown in Figure 4. In the JBW zeolite (1 M NaOH), broad O–H stretching bands at 3400–3530 cm^{-1} and H–O–H bending bands at 1640–1670 cm^{-1} were observed, corresponding to adsorbed or confined water molecules within the zeolitic pores. Framework vibrations in the 900-1200 cm^{-1} region, assigned to T–O–T stretching, were recorded and considered diagnostic of the JBW structure. Additional features in the 400–800 cm^{-1} region, including double-ring (D4R/D6R) modes and Si–O/Al–O linkages, further confirmed the formation of JBW-type zeolite. A strong band at 960–965 cm^{-1}, together with features at 420–500 cm^{-1} and a weak band at 760–770 cm^{-1}, was attributed to asymmetric T–O–T vibrations, double-ring modes, and the fingerprint region of JBW (Vogrin et al., 2023). In the pure ZnO, a strong absorption at 445–523 cm^{-1} was attributed to Zn–O stretching vibrations, by which the formation of crystalline ZnO was confirmed (Khan et al., 2025). A wide absorption feature at 3148 cm^{-1} was assigned to the O–H stretching vibration of surface –OH groups and physically adsorbed water (Shukla et al., 2025). In the ZnO/JBW composite Figure 5b, overlapping bands in the 472-680 cm^{-1} region indicated Zn-O vibrations superimposed on the JBW framework. The absorption feature at 1111 cm^{-1} is attributed to the asymmetric vibration of the Si–O–Si/Al–O linkages, while the bands observed within 993–799 cm^{-1} indicate that the structural integrity of the JBW framework remained intact. Broad features at 3498–1645 cm^{-1} reflected the presence of hydroxyl groups and water molecules confined within the zeolite pores. These findings were consistent with the XRD result, suggesting that ZnO integration did not disrupt the JBW framework but instead enhanced interfacial interactions. Previous studies have reported (Munguti et al., 2023), that the incorporation of ZnO into

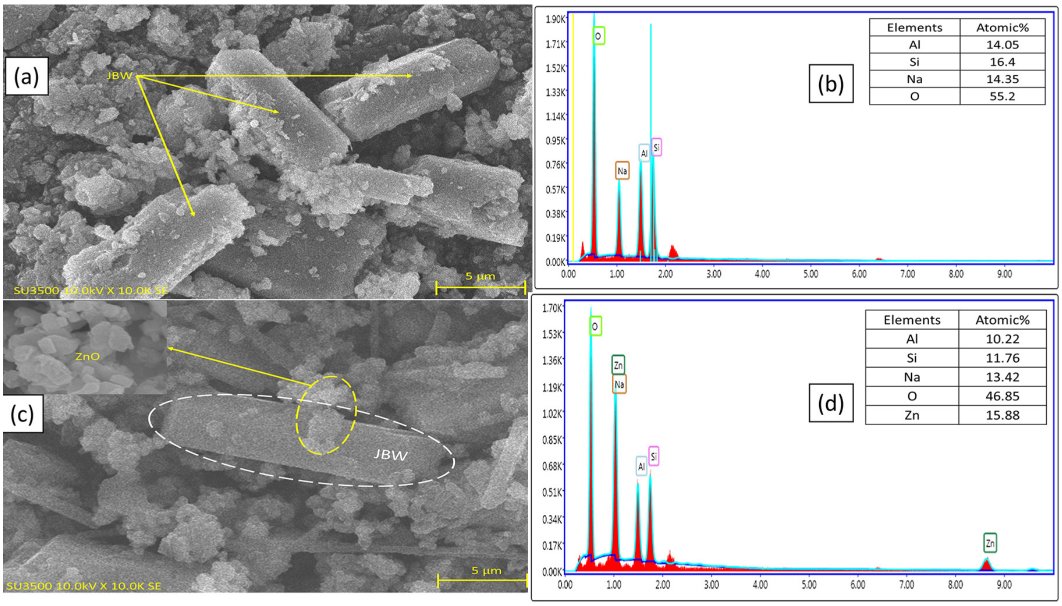

Elements	Atomic%
Al	14.05
Si	16.4
Na	14.35
O	55.2

Elements	Atomic%
Al	10.22
Si	11.76
Na	13.42
O	46.85
Zn	15.88

Figure 3. SEM–EDX generated images and corresponding tables present the elemental composition of (a–b) JBW and (c–d) ZnO/JBW composite

a zeolite matrix improves structural integrity and introduces active surface sites beneficial for photocatalytic applications.

Textural properties (BET and BJH)

The textural characteristics of the produced materials were assessed using nitrogen adsorption–desorption measurements (Figure 5). The JBW zeolite exhibited a type IV isotherm with an H3 hysteresis loop, whereas the ZnO/JBW composite displayed a type III isotherm. A summary of the BET results presented in Table 2 shows pore sizes > 2 nm, indicating a mesoporous structure, as well as an increase in surface area from 14.15 m²/g for JBW to 26.22 m²/g for ZnO/JBW. In addition, the pore volume also increased significantly compared to the JBW sample. Prior studies have shown analogous behavior for ZnO when incorporated into zeolite matrices (Baldez et al., 2024; Santos et al., 2023)

The BJH pore size distribution (Figure 5a and Figure 5b) further confirms the presence of mesopores in ZnO/JBW centered at approximately 11 nm, while JBW exhibits a main peak at around 12 nm. The literature has reported comparable findings for ZnO–zeolite composite materials, where the presence of hierarchical porosity facilitated molecular diffusion and improved the accessibility of active sites, thereby enhancing photocatalytic performance (Healey et al., 2000; Lin et al., 2004; Yu et al., 2024). The observed increase in surface area and pore volume indicated that ZnO/JBW possessed superior textural properties, suggesting greater potential for photocatalytic applications. The enhanced mesoporosity was expected to facilitate mass transport and support higher catalytic efficiency, in agreement with previous reports on ZnO/zeolite-based systems (Munguti et al., 2023).

Thermal characterization (TGA-DSC)

The thermal behavior of materials was evaluated by thermogravimetric analysis (TGA) and differential scanning calorimetry (DSC) to evaluate thermal stability and associated transition mechanisms, as shown in Figure 6. From the TGA curve of the JBW sample (Figure 6a), a total weight loss of 7.00% was recorded in two main steps. The first stage, with a mass loss of 3.96% was observed within the temperature range of 50–200 °C and was attributed to the release of physisorbed water molecules from the zeolite pores. This event was accompanied by a broad endothermic peak in the DSC curve (Figure 6b), centered at 262.85 °C, corresponding to dehydration and dihydroxylation signals typical of zeolitic frameworks. A second-stage mass loss of 3.04% was recorded up to 500 °C, indicating partial degradation of the structural hydroxyl groups. The corresponding DSC signal displayed a peak at 286/80

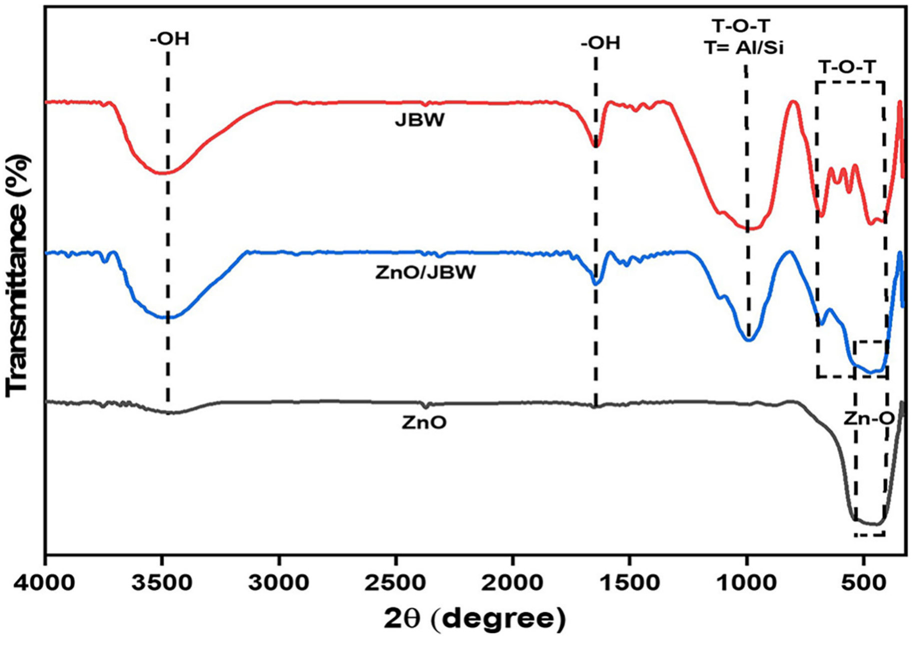

Figure 4. FTIR Spectra of ZnO, JBW, and the ZnO/JBW composite

Table 2. Surface area and porosity of JBW and ZnO/JBW composite

Sampel	BET surface area (m^2/g)	Total pore volume (cm^3/g)	Average pore size (nm)
JBW	14.15	0.039	11.12
ZnO/JBW	26.22	0.079	12.10

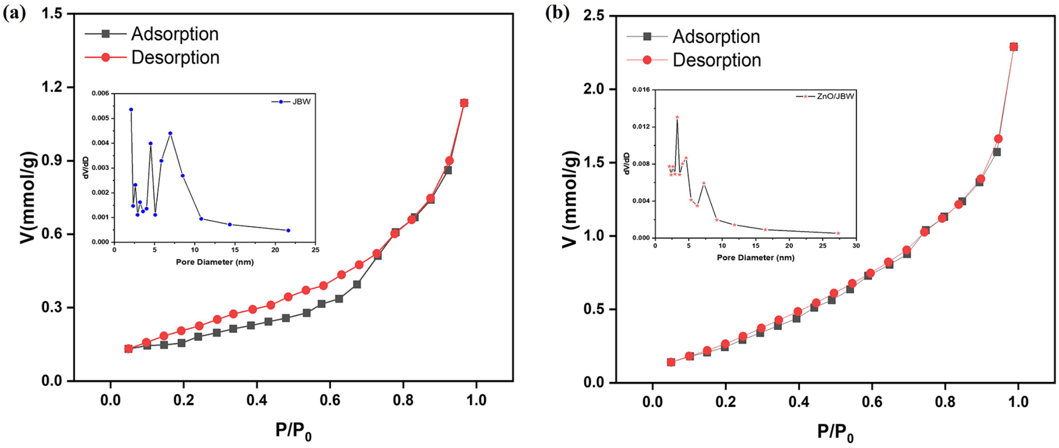

Figure 5. N_2 adsorption–desorption isotherm and BJH pore-size distribution for a) zeolite JBW and b) ZnO/JBW composite

°C, with ΔH of 73.54 J/g, which confirmed the energy involved in the structural transition. These results were consistent with previous reports (Asselman et al., 2022; Vogrin et al., 2023), which described the gradual dehydration of zeolites at low to moderate temperatures (<350 °C) prior to the weakening of the aluminosilicate framework at elevated temperatures.

The ZnO (Figure 6a) TGA profile revealed high thermal stability, with only 0.30% mass loss. The DSC curve (Figure 6b) showed minimal energy transitions, characterized by an endothermic signal with an onset at 176.3 °C and a peak at 228 °C, corresponding to a ΔH of 10.59 J/g, attributed to the release of superficial moisture. A second peak observed at 582.7 °C with ΔH = 1.69 J/g was associated with ZnO lattice relaxation. In contrast, the ZnO/JBW composite exhibited a combined thermal behavior both constituent materials. A total mass loss of 4.40% was recorded in the TGA profile, with the initial stage 50–300 °C corresponding to the release of pore confined water, followed by structural changes at the interface occurring in the range 300–600 °C. These findings were further supported by the DSC curve, which displayed two distinct thermal events: an endothermic peak at 273.1 °C with ΔH = 28.87 J/g, attributed to the structural dehydration of JBW, and an exothermic peak at 508.6 °C with ΔH = -8.51 J/g, indicating crystal reorganization at the ZnO/JBW interface. Compared to JBW, the ZnO/JBW composite exhibited a lower dehydration enthalpy, indicating reduced water retention due to the incorporation of ZnO. The shift in high-temperature transitions confirmed the enhanced thermal stability of the JBW framework, attributed to the ZnO structural buffering effect, as previously reported (Khaleque et al., 2020; Soliman et al., 2022; H. Wang et al., 2020). TGA-DSC results revealed that while JBW showed high water adsorption but poor thermal resistance, ZnO was highly stable with minimal energy transitions. The composite combined both traits, offering significant water retention and improved thermal stability, supporting its potential for photocatalytic applications.

Optical properties (UV-DRS)

The UV-Vis absorption spectra of ZnO and ZnO/JBW are presented in Figure 7a. For ZnO, an absorption edge at approximately 368 nm was observed, which has been recognized as a typical feature of semiconductor band-to-band transitions. After composite with JBW zeolite, an increase in absorption intensity and a noticeable extension into the visible region were detected in the ZnO/JBW sample. Superior optical performance

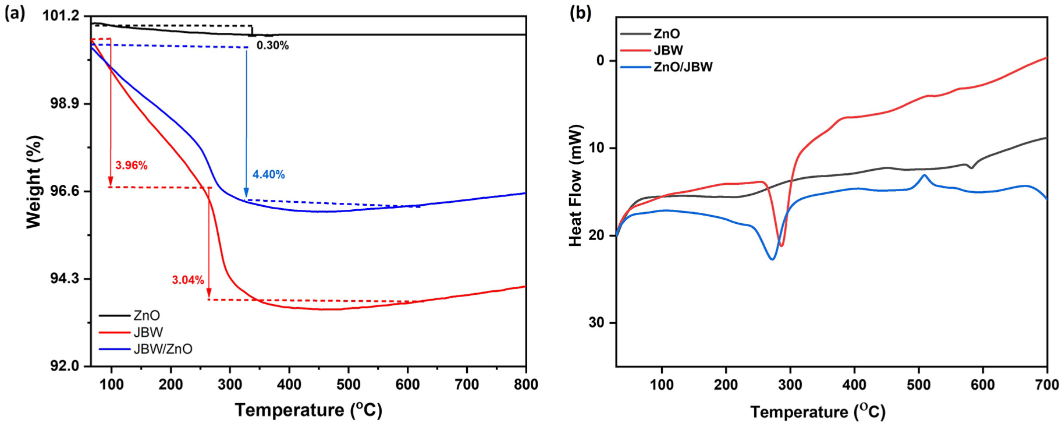

Figure 6. TGA (a) and DSC (b) curves of Z JBW, and ZnO/JBW composite

compared to pure ZnO was achieved through improved ZnO dispersion and stronger light-matter interactions, which were facilitated by the JBW framework (Wang et al., 2024).

The optical band gaps were evaluated by applying the Kubelka–Munk transformation and Tauc plot analysis, as illustrated in Figure 7b. A narrower band gap of 3.12 eV was obtained for ZnO/JBW, compared to 3.18 eV for pure ZnO. Although this shift is modest, it can significantly influence photocatalytic activity because a narrower band gap lowers the excitation energy required for photogenerated electron–hole pair formation, thereby enhancing light utilization. Furthermore, intimate interfacial contact between ZnO and the JBW zeolite support facilitates directional charge transfer driven by interfacial band alignment, thereby suppressing electron–hole recombination and improving charge-separation efficiency, as commonly observed in heterojunction photocatalysts (Sohail et al., 2024).

Therefore, the improved photocatalytic behavior of ZnO/JBW is not governed solely by band-gap narrowing, but also by synergistic effects involving enhanced light absorption, interfacial charge transfer, and the porous zeolitic framework. Consistent with the literature, oxide–zeolite composites were found to improve photocatalytic efficiency by optimizing light utilization and pore structure (Bilal et al., 2025; Packialakshmi et al., 2023). In conjunction with the presented data, these findings suggest that ZnO/JBW possesses promising photocatalytic characteristics. Based on the given result, ZnO/JBW was identified as a promising material for photocatalytic applications.

Effect of pH on photocatalytic activity

The effect of pH on the photocatalytic degradation of materials after 60 min of mercury lamp irradiation with a starting concentration of RhB of 25 mg/Lof 25 mg/L is presented in Figure

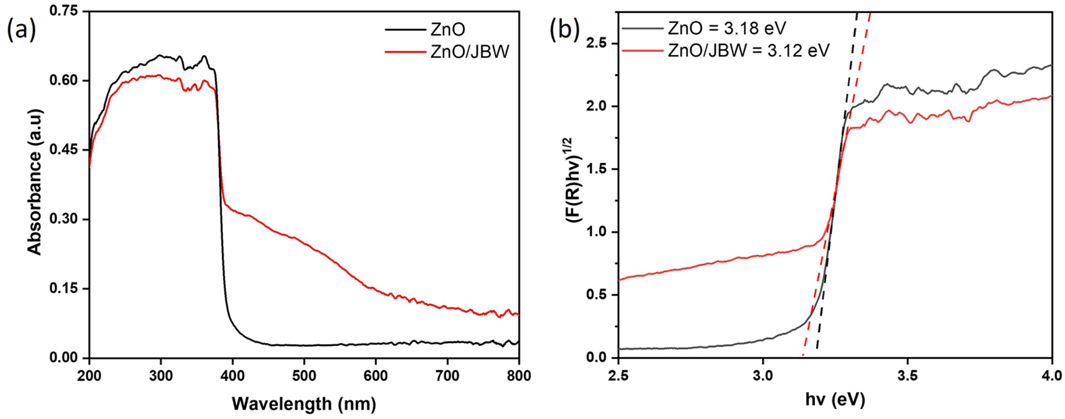

Figure 7. UV-DRS of ZnO and ZnO/JBW (a) absorbance spectrum and (b) band gap energy calculation using the Kubelka-Munk method

8. A significant variation in degradation efficiency was observed among the three systems. For JBW, the degradation efficiency remained relatively constant at 40–50%, with the highest value recorded at pH 6 (49.84± 0.0030%). This behavior indicated that the removal was dominated by adsorption on the zeolitic framework, which was less sensitive to pH fluctuations. In the case of ZnO, the degradation efficiency exhibited a stronger dependence on pH. The highest performance was observed at pH 8 (42.86 ± 0.0046%), while a sharp decline was recorded at pH 9 (20.73 ± 0.0032%). This trend is consistent with the reported point of zero charge (pHpzc) of ZnO (7–9), where at higher alkaline pH, excessive hydroxyl ions hindered surface activity and reduced photocatalytic efficiency (El Golli et al., 2023).

The ZnO/JBW composite consistently outperformed both single materials, achieving degradation efficiencies above 75% across all pH values. The maximum removal (83.45± 0.0076%) was obtained at pH 8, followed by 80.39± 0.0021% at pH 9. The enhancement can be attributed to the synergistic effect of JBW in dispersing ZnO, providing additional adsorption sites, and reducing electron–hole recombination, a phenomenon that has been similarly reported for other zeolite–ZnO systems (Kabadayi et al., 2024). The results indicated that ZnO/JBW composites exhibited the most robust and efficient photocatalytic performance, particularly at mildly alkaline pH levels. In contrast, ZnO alone exhibited strong pH sensitivity, whereas JBW primarily served as a stable adsorbent.

Effect of initial RhB concentration

The effect of the initial RhB concentration on the photocatalytic degradation efficiency using ZnO, JBW, and the ZnO/JBW composite is shown in Figure 9. The results indicate that increasing the initial RhB concentration leads to a decrease in degradation efficiency for all materials. A gradual decline in degradation efficiency was observed as the initial dye concentration increased from 10 to 35 mg/L during 60 minutes of irradiation. This decrease is attributed to the saturation of the catalyst's active sites and the reduced light penetration caused by the higher RhB concentration, which limits the generation of reactive oxygen species.

The ZnO efficiency decreased from 64.07 ± 0.0025% at 10 mg/L to 27.40 ± 0.0235% at 35 mg/L, whereas JBW exhibited a decline from 67.83 ± 0.0055% to 20.47 ± 0.0032% under the same conditions, confirming its primarily adsorptive role. In contrast, the ZnO/JBW composite exhibited superior performance, achieving 97.33 ± 0.0006% degradation at 10 mg/L and maintaining 75.02 ± 0.0015% at 35 mg/L. This enhanced performance is attributed to the synergistic effect

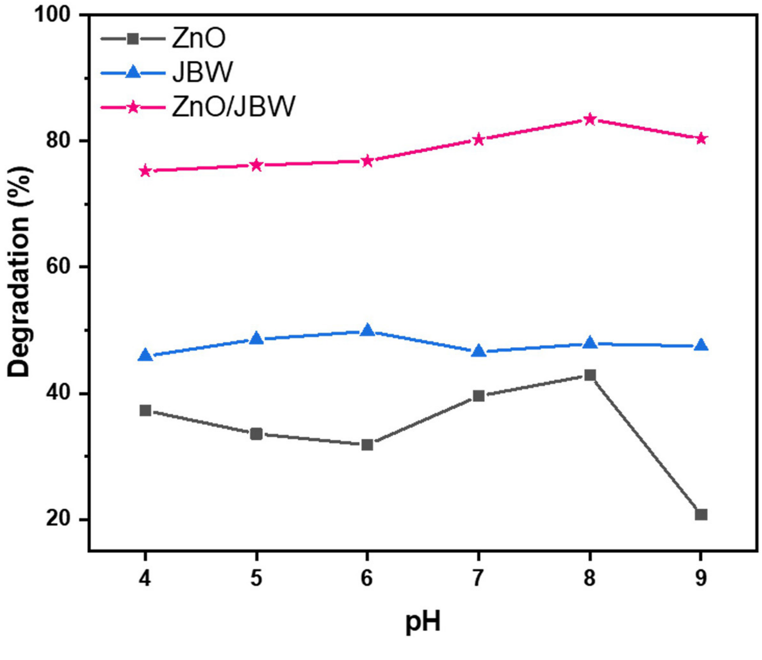

Figure 8. Effect of pH (4–9) on the photocatalytic performance of ZnO, JBW, and ZnO/JBW composite

between the two components, where JBW zeolite facilitates the pre-concentration of RhB molecules around the active sites of ZnO, while ZnO acts as a photocatalyst that promotes oxidation through the generation of reactive oxygen species (Mugumo et al., 2023). Based on these results, optimum concentrations of 20 mg/L for ZnO and ZnO/JBW, and 15 mg/L for JBW, were identified as the most effective conditions for RhB removal, achieving degradation efficiencies of 61.37 ± 0.0026%, 94.34 ± 0.0016%, and 60.32 ± 0.0010%, respectively.

Effect of light irradiation period on degradation

The influence of exposure time on RhB photocatalytic degradation using JBW, ZnO, and the ZnO/JBW composite is illustrated in Figure 10a. All materials exhibited a gradual increase in degradation efficiency with longer irradiation periods, with the highest performance observed at 150 minutes.

The ZnO/JBW composite showed the highest performance, achieving 97.83% ± 0.0030% degradation compared with 65.81% ± 0.0015% for ZnO and 58.74% ± 0.0010% for JBW. This superior activity can be attributed to the synergistic effect between the adsorption capacity of JBW and the photocatalytic activity of ZnO. The JBW framework serves as an adsorptive matrix that preconcentrates RhB molecules near ZnO active sites, thereby increasing the probability of photocatalytic reactions. Meanwhile, ZnO functions as the photocatalytic center, generating reactive oxygen species under UV irradiation that effectively cleave the chromophoric bonds in the dye molecules.

The changes observed in the UV–Vis spectra of RhB throughout its photocatalytic degradation by the ZnO/JBW composite, as illustrated in Figure 10b, provide additional confirmation of these results. A gradual decrease in the characteristic absorption peak at 554–555 nm was observed as the irradiation time increased, with the peak almost disappearing after 150 minutes. This continuous reduction in absorbance closely correlates with the decrease in RhB concentration in solution, confirming the high degradation efficiency determined experimentally. The lack of notable signals detected in the visible spectrum indicates that the degradation primarily proceeds via direct mineralization rather than the accumulation of stable intermediates, consistent with previous reports on ZnO/zeolite-based photocatalysts (Hu et al., 2023). Overall, these results demonstrate that the ZnO/JBW composite achieves a faster degradation equilibrium and maintains a higher overall efficiency than its individual components, thereby confirming the potential of the ZnO/JBW composite as a robust candidate for practical wastewater treatment applications.

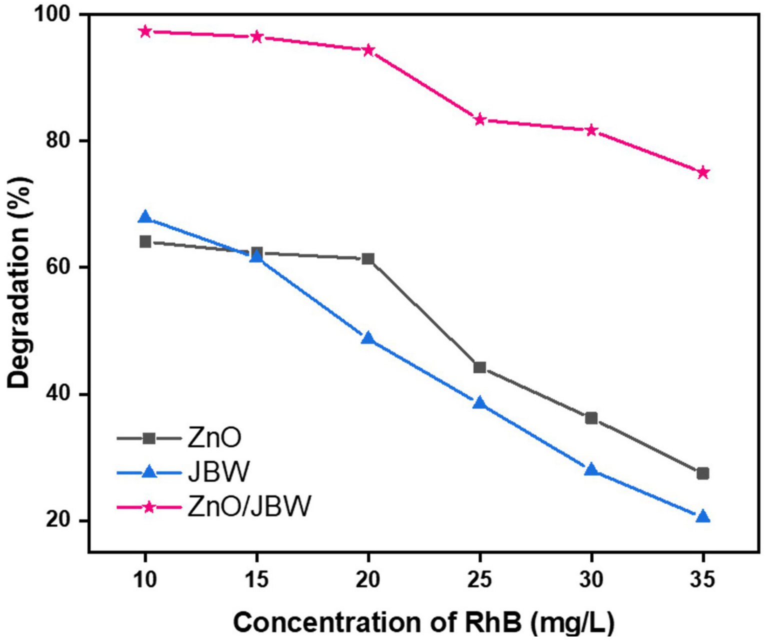

Figure 9. Effect of initial RhB concentration (10–35 mg/L) on ZnO, JBW, and ZnO/JBW composite

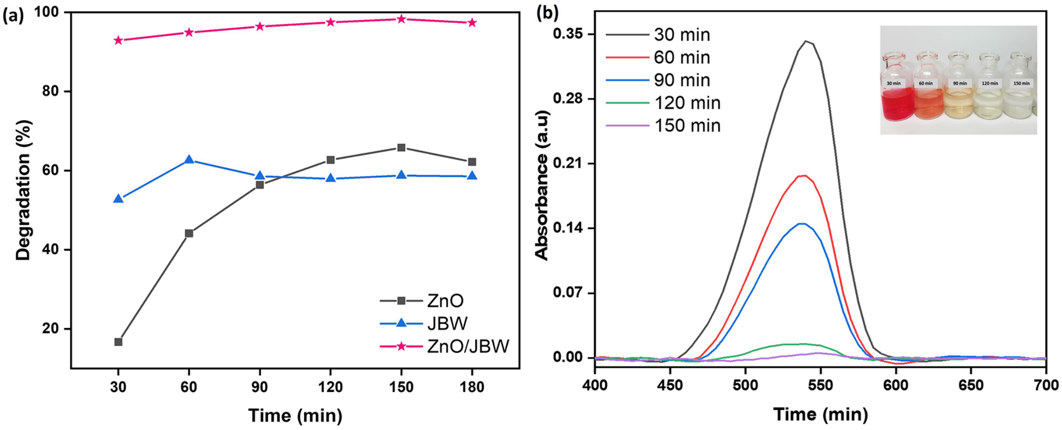

Figure 10. Photocatalytic performance of ZnO, JBW, and ZnO/JBW composite for RhB degradation under UV a) effect of irradiation time (30-180 minutes) and b) UV–vis spectra and visual color change during degradation

Photocatalytic degradation efficiency under optimum conditions

Photocatalytic degradation experiments were conducted under the previously optimized conditions of pH, initial dye concentration, and irradiation time to evaluate the maximum performance of ZnO, JBW, and the ZnO/JBW composite.

The results in Figure 11 show that The ZnO/JBW composite exhibited the highest degradation efficiency, reaching 98,23 ± 0.0021%, which was significantly higher than that of pure ZnO (65.81 ± 0.0032%) and JBW (58.74 ± 0.0036%). The enhanced performance of the ZnO/JBW composite arises from the synergistic effect of its components: JBW zeolite acts as an adsorbent, concentrating RhB molecules near the ZnO surface and thereby accelerating the oxidation process, while ZnO serves as the photocatalyst. These findings demonstrate the potential of the ZnO/JBW composite as a promising candidate for practical wastewater treatment applications.

To further confirm this enhanced performance, a comparison of RhB photodegradation efficiencies of various ZnO-based materials reported in previous studies is summarized in Table 3. The comparison was conducted based on several factors, including photocatalyst type,

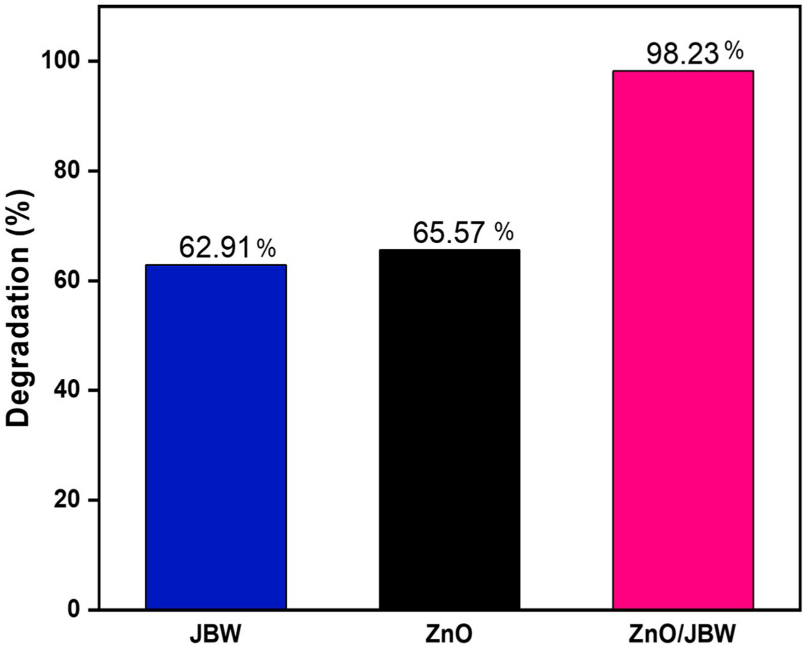

Figure 11. Photocatalytic degradation efficiency of JBW, ZnO, and ZnO/JBW composites under optimal conditions

Table 3. Comparison of photodegradation of Rhodamine B by ZnO-based materials

Photocatalysts	Catalyst loading (g/L)	Concentration of RhB (mg/L)	Reaction time (minutes)	Degradation efficiency (%)	Reference
ZnO/Vietnamese MMT	0.1	10	210	95.5	(Dao et al., 2023)
ZnO/BP/C_3N_4	0.01	5	80	97	(Moradian et al., 2023)
ZnO/zeolite	0.1	5	80	81	(Alakhras et al., 2020)
CuO/Fe_2O_3/ZnO	1	2	120	88.8	(Jansanthea et al., 2024)
ZnO/CuO	0.1	10	180	98	(Truong et al., 2022)
ZnO/JBW	0.1	20	150	98.23	This work

catalyst loading, pollutant concentration, irradiation time, and Degradation efficiency. The results show that ZnO/JBW exhibits enhanced separation efficiency even at relatively high RhB concentrations. These findings confirm the potential of ZnO/JBW as an effective photocatalyst for wastewater treatment applications.

CONCLUSIONS

In this study, JBW zeolite was successfully synthesized from feldspar Gowa, South Sulawesi using the hydrothermal method and then composited with ZnO. XRD and FTIR characterization results showed the formation of a stable JBW framework, while SEM-EDS revealed that ZnO was evenly dispersed on the zeolite surface. BET and BJH analyses revealed increased surface area and mesoporosity in the composite, and TGA/DSC showed better thermal stability than pure JBW. Furthermore, the ZnO/JBW composite has a narrower optical band gap and higher light absorption capacity than pure ZnO. Photocatalytic studies also show that this composite performs better than JBW or ZnO alone under various pH conditions, initial RhB concentrations, and irradiation times. Under optimized conditions, a maximum RhB degradation efficiency of 98.23 ± 0.0021% was attained by the ZnO/JBW composite, attributed to the synergistic combination of JBW adsorption capacity and ZnO photocatalytic activity.

Acknowledgments

The authors gratefully acknowledge the Lembaga Pengelola Dana Pendidikan (LPDP), Ministry of Finance of the Republic of Indonesia, for providing scholarship support and financial assistance for this research

REFERENCES

1. Aina, A. R. N., Patel, H., Aich, S., Roy, B., Samanta, N. S., Pal, B. (2025). Recent advances in ZnO based photocatalysts for industrial dye degradation. *Discover Applied Sciences*, *7,* 977. https://doi.org/10.1007/s42452-025-07530-z
2. Al-Buriahi, A. K., Al-Gheethi, A. A., Senthil Kumar, P., Radin Mohamed, R. M. S., Yusof, H., Alshalif, A. F., Khalifa, N. A. (2022). Elimination of rhodamine B from textile wastewater using nanoparticle photocatalysts: A review for sustainable approaches. *Chemosphere*, *287,* 132162. https://doi.org/10.1016/j.chemosphere.2021.132162
3. Al-Tohamy, R., Ali, S. S., Li, F., Okasha, K. M., Mahmoud, Y. A. G., Elsamahy, T., Jiao, H., Fu, Y., Sun, J. (2022). A critical review on the treatment of dye-containing wastewater: Ecotoxicological and health concerns of textile dyes and possible remediation approaches for environmental safety. *Ecotoxicology and Environmental Safety*, *231*, 113160. https://doi.org/10.1016/j.ecoenv.2021.113160
4. Alakhras, F., Alhajri, E., Haounati, R., Ouachtak, H., Addi, A. A., Saleh, T. A. (2020). A comparative study of photocatalytic degradation of Rhodamine B using natural-based zeolite composites. *Surfaces and Interfaces*, *20*, 100611. https://doi.org/10.1016/j.surfin.2020.100611
5. Asselman, K., Radhakrishnan, S., Pellens, N., Chandran, C. V., Houlleberghs, M., Xu, Y., Martens, J. A., Sree, S. P., Kirschhock, C. E. A., Breynaert, E. (2022). HSIL-based synthesis of ultracrystalline K,Na-JBW, a zeolite exhibiting exceptional framework ordering and flexibility. *Chemistry of Materials*, *34*(16), 7159–7166. https://doi.org/10.1021/acs.chemmater.2c01059
6. Baldez, W. M. C., Santos, J. D. J. P., Santos, W. D. C., Aguilar-Pliego, J., Martín, N., Cabral, A. A., Paiva, A. E. M., Rodrigues, S. F., Teixeira, M. M., Alcântara, A. C. S., Rojas, A. (2024). Enhanced photodegradation of ciprofloxacin antibiotic using ZnO@FAU composite: A promising material for contaminant removal. *Desalination and Water Treatment*, *318*. https://doi.org/10.1016/j.dwt.2024.100356

7. Bekele, E. A., Korsa, H. A., Desalegn, Y. M., Bekele, G. G. (2025). Optimization of binary ZnO/rGO nanocomposite for enhanced photocatalytic degradation of rhodamine B dye using response surface methodology. *Journal of Alloys and Compounds*, *1041*, 183779. https://doi.org/10.1016/j.jallcom.2025.183779
8. Bilal, A. S. S., Khan, M. U. A., Banik, N., Hayitov, A., MM, R., Ray, S., Ghai, K., Singh, U., Khudoynazarov, E., Aleem, M., Qureshi, A. A. (2025). Dual-doped ZnO nanocomposites for superior photocatalytic hydrogen generation. *Journal of Materials Science: Materials in Engineering*, *20*, 104. https://doi.org/10.1186/s40712-025-00327-3
9. Dao, T. T. B., Ha, L. T. T., Nguyen, D. T., Le, N. H., Luu, Q. K., Nguyen, T. H., Ha-Thuc, C.-N. (2023). Vietnamese montmorillonite supported ZnO: preparation, characterization, and photocatalytic enhancement in degradation of Rhodamine B. *Kinetics and Catalysis*, *64*(4), 390–402. https://doi.org/10.1134/S002315842304002X
10. de Dios, F. S., Morales, E. R., Del Carmen Arellano Cortaza, M., Hernández, G. P., Mandujano, E. V. M., Alejandro, E. M. L., Blanco, L. R. (2023). Improvement of photocatalysis using ZnO/zeolite nanocomposites for contaminant removal in aqueous media. *Desalination and Water Treatment*, *312*, 79–88. https://doi.org/10.5004/dwt.2023.29961
11. El Golli, A., Contreras, S., Dridi, C. (2023). Biosynthesized ZnO nanoparticles and sunlight-driven photocatalysis for environmentally-friendly and sustainable route of synthetic petroleum refinery wastewater treatment. *Scientific Reports*, *13*(1), 1–14. https://doi.org/10.1038/s41598-023-47554-2
12. Fatimah, H., Taba, P., Fauziah, S., Karim, A., Liong, S., Kasim, S., Sahrul, Pardan, N. A. (2025). Removal of methyl violet dye by a photocatalytic process using variations of TiO_2/zeolite synthesized from muscovite raw material. *Journal of Ecological Engineering*, *26*(5), 73–86. https://doi.org/10.12911/22998993/200503
13. Goodarzi, N., Ashrafi-Peyman, Z., Khani, E., Moshfegh, A. Z. (2023). Recent progress on semiconductor heterogeneous photocatalysts in clean energy production and environmental remediation. *Catalysts*, *13*(7). https://doi.org/10.3390/catal13071102
14. Healey, A. M., Johnson, G. M., Weller, M. T. (2000). Synthesis and characterization of JBW-type zeolites. Part A: Sodium/potassium aluminosilicate, $Na_2K[Al_3Si_3O_{12}]\cdot 0.5H_2O$. *Microporous and Mesoporous Materials*, *37*(1), 153–163. https://doi.org/10.1016/S1387-1811(99)00262-0
15. Hegazy, E. Z., Kosa, S. A., Abd El Maksod, I. H. (2012). Synthesis and characterization of JBW structure and its thermal transformation. *Journal of Solid State Chemistry*, *196*, 150–156. https://doi.org/10.1016/j.jssc.2012.06.014
16. Hu, T., Li, J., Wang, L., Wang, H., Zhang, Z., Jiang, W., Xue, C. (2023). $ZnO/ZnFe_2O_4$/zeolite composite catalyst for peroxymonosulfate oxidation and photocatalysis. *Materials Letters*, *330*, 133310. https://doi.org/10.1016/j.matlet.2022.133310
17. Hübner, U., Spahr, S., Lutze, H., Wieland, A., Rüting, S., Gernjak, W., Wenk, J. (2024). Advanced oxidation processes for water and wastewater treatment – Guidance for systematic future research. *Heliyon*, *10*(9), e30402. https://doi.org/10.1016/j.heliyon.2024.e30402
18. Imessaoudene, A., Mechraoui, O., Aberkane, B., Benabbas, A. (2024). Nano-structures & nano-objects synthesis of a TiO_2/zeolite composite : Evaluation of adsorption-photodegradation synergy for the removal of Malachite Green. *Nano-Structures & Nano-Objects*, *38*. https://doi.org/10.1016/j.nanoso.2024.101191
19. Jansanthea, P., Inyai, N., Chomkitichai, W., Ketwaraporn, J., Ubolsook, P., Wansao, C., Wanaek, A., Wannawek, A., Kuimalee, S., Pookmanee, P. (2024). Green synthesis of CuO/Fe_2O_3/ZnO ternary composite photocatalyst using grape extract for enhanced photodegradation of environmental organic pollutant. *Chemosphere*, *351*, 141212. https://doi.org/10.1016/j.chemosphere.2024.141212
20. Kabadayi, O., Altintig, E., Ballai, G. (2024). Zeolite supported zinc oxide nanoparticles composite: Synthesis, characterization, and photocatalytic activity for methylene blue dye degradation. *Desalination and Water Treatment*, *319*, 100433. https://doi.org/10.1016/j.dwt.2024.100433
21. Khaleque, A., Alam, M. M., Hoque, M., Mondal, S., Haider, J. Bin, Xu, B., Johir, M. A. H., Karmakar, A. K., Zhou, J. L., Ahmed, M. B., Moni, M. A. (2020). Zeolite synthesis from low-cost materials and environmental applications: A review. *Environmental Advances*, *2*. 100019. https://doi.org/10.1016/j.envadv.2020.100019
22. Khan, A., Chen, H. Y., Rusly, C. (2025). Visible-light-driven removal of mixed dye pollutants by a novel ZnO/CNT/GO ternary nanocomposite: Synergistic degradation of Congo red and methylene blue. *Environmental Research*, *283*, 122156. https://doi.org/10.1016/j.envres.2025.122156
23. Lin, D. C., Xu, X. W., Zuo, F., Long, Y. C. (2004). Crystallization of JBW, CAN, SOD and ABW type zeolite from transformation of meta-kaolin. *Microporous and Mesoporous Materials*, *70*(1–3), 63–70. https://doi.org/10.1016/j.micromeso.2004.03.003
24. Moradian, S., Mohammadi Ziarani, G., Badiei, A., Iravani, S. (2023). ZnO/black phosphorus/C_3N_4 composite: An effective photocatalyst for Cr (VI) reduction and degradation of rhodamine B. *Environmental Research*, *238*, 117122. https://doi.org/10.1016/j.envres.2023.117122

25. Mugumo, R., Ichipi, E., Tichapondwa, S. M., Chirwa, E. M. N. (2023). Visible-light-induced photocatalytic degradation of Rhodamine B dye using a CuS/ZnS p-n heterojunction nanocomposite under visible-light irradiation. *Catalysts*, *13*(8). https://doi.org/10.3390/catal13081184
26. Munguti, L. K., Dejene, F. B., Muthee, D. K. (2023). High photodegradation performance of ZnO nanoparticles supported on porous Zeolite Na-A: Effects of ZnO loading. *Materials Chemistry and Physics*, *295*, 127063. https://doi.org/10.1016/j.matchemphys.2022.127063
27. Packialakshmi, J. S., Albeshr, M. F., Alrefaei, A. F., Zhang, F., Liu, X., Selvankumar, T., Mythili, R. (2023). Development of ZnO/SnO_2/rGO hybrid nanocomposites for effective photocatalytic degradation of toxic dye pollutants from aquatic ecosystems. *Environmental Research*, *225*, 115602. https://doi.org/10.1016/j.envres.2023.115602
28. Rajendran, R., Rojviroon, O., Arumugam, P., Ramasamy, G., Paramasivam, S., Rojviroon, T. (2025). Synergistic effects of activated Carbon-Supported TiO_2/ZnO nanocomposites for photocatalytic dye degradation and antibacterial activity. *Journal of Molecular Liquids*, *433*, 127792. https://doi.org/10.1016/j.molliq.2025.127792
29. Santos, W. D. C., Teixeira, M. M., Campos, I. R., de Lima, R. B., Mantilla, A., Osajima, J. A., de Menezes, A. S., Manzani, D., Rojas, A., Alcântara, A. C. S. (2023). Photocatalytic degradation of ciprofloxacin using semiconductor derived from heterostructured ZIF-8-based materials. *Microporous and Mesoporous Materials*, *359*. https://doi.org/10.1016/j.micromeso.2023.112657
30. Shamsaei, E., Basquiroto de Souza, F., Sagoe-Crentsil, K., Duan, W. (2022). ZIF-8 derived ZnO–calcium silicate mesoporous structures: Synthesis and photocatalytic activity. *Microporous and Mesoporous Materials*, *332*, 111702. https://doi.org/10.1016/j.micromeso.2022.111702
31. Shukla, S., Sharma, A., Rathi, G., Manchanda, A., Khan, A., Malik, M. A., Chaudhry, S. A. (2025). Facile fabrication of novel Y-doped ZnO biochar-based nanocomposite for efficient removal of Sulfasalazine, Congo red and Bismarck brown-R: Insight into adsorption performance and mechanism. *Surfaces and Interfaces*, *71*, 106817. https://doi.org/10.1016/j.surfin.2025.106817
32. Singh, N., Sharma, D., Thakur, M., Dan, A. (2025). Zinc oxide-loaded chitosan-graphene oxide hydrogel nanocomposite as a potential catalyst for photocatalytic dye degradation. *International Journal of Biological Macromolecules*, *308*(P4), 142424. https://doi.org/10.1016/j.ijbiomac.2025.142424
33. Skjolding, L. M., Jørgensen, L. v. G., Dyhr, K. S., Köppl, C. J., McKnight, U. S., Bauer-Gottwein, P., Mayer, P., Bjerg, P. L., Baun, A. (2021). Assessing the aquatic toxicity and environmental safety of tracer compounds Rhodamine B and Rhodamine WT. *Water Research*, *197*, 117109. https://doi.org/10.1016/j.watres.2021.117109
34. Soliman, A. I. A., Abdel-Wahab, A. M. A., Abdelhamid, H. N. (2022). Hierarchical porous zeolitic imidazolate frameworks (ZIF-8) and ZnO@N-doped carbon for selective adsorption and photocatalytic degradation of organic pollutants. *RSC Advances*, *12*(12), 7075–7084. https://doi.org/10.1039/d2ra00503d
35. Truong, T. T., Pham, T. T., Truong, T. T. T., Pham, T. D. (2022). Synthesis, characterization of novel ZnO/CuO nanoparticles, and the applications in photocatalytic performance for rhodamine B dye degradation. *Environmental Science and Pollution Research*, *29*(15), 22576–22588. https://doi.org/10.1007/s11356-021-17106-0
36. Vogrin, J., Santini, T., Peng, H., Zhao, L., Vaughan, J. (2023). Synthesis of zeolites using kaolin in concentrated sodium hydroxide-aluminate solutions. *Applied Clay Science*, *244*, 107106. https://doi.org/10.1016/j.clay.2023.107106
37. Wang, H., Wang, L., Xiao, F. S. (2020). Metal@zeolite hybrid materials for catalysis. *ACS Central Science*, *6*(10), 1685–1697. https://doi.org/10.1021/acscentsci.0c01130
38. Wang, J., Song, Q., Zhou, X., Li, R., He, Q., Wang, J., Yang, H., Duan, H., Li, L. (2024). Preparation of fly ash zeolite supported ZnO/Co_3O_4 catalyst for the photocatalytic degradation of xanthate under visible light. *Optical Materials*, *157*, 116262. https://doi.org/10.1016/j.optmat.2024.116262
39. Wei, Y., Lei, E., Chen, Y., Zhao, D., Li, J., Lv, Y., Wei, H. (2025). A novel heterojunction material of TiO2/ZnO/$ZnTiO_3$ with excellent photocatalytic activity for dye degradation. *Materials Letters*, *391*. https://doi.org/10.1016/j.matlet.2025.138507
40. Yan, L., Chen, S., Wang, P., Liu, X., Han, L., Yan, T., Li, Y., Zhang, D. (2024). Hydrothermally stable metal oxide-zeolite composite catalysts for low-temperature NOx reduction with improved N_2 selectivity. *Chinese Chemical Letters*, *35*(6), 109132. https://doi.org/10.1016/j.cclet.2023.109132
41. Yu, T., Zheng, J., Su, S., Wang, Y., Xu, J., Liu, Z. (2024). Zinc Oxide nanoclusters encapsulated in MFI zeolite as a highly stable adsorbent for the ultradeep removal of hydrogen sulfide. *Journal of the American Chemical Society*, *4*(3), 985–991. https://doi.org/10.1021/jacsau.3c00733